

ESI, a New Keck Observatory Echelle Spectrograph and Imager

A. I. SHEINIS,¹ M. BOLTE,¹ H. W. EPPS,¹ R. I. KIBRICK,¹ J. S. MILLER,¹ M. V. RADOVAN,¹ B. C. BIGELOW,² AND B. M. SUTIN²

Received 2002 January 10; accepted 2002 April 15; published 2002 July 10

ABSTRACT. The Echelle Spectrograph and Imager (ESI) is a multipurpose instrument that has been delivered by the Instrument Development Laboratory of Lick Observatory for use at the Cassegrain focus of the Keck II telescope. ESI saw first light on 1999 August 29. ESI is a multimode instrument that enables the observer to seamlessly switch between three modes during an observation. The three modes of ESI are an $R = 13,000$ echelle mode, a low-dispersion prismatic mode, and a direct-imaging mode. ESI contains a unique flexure compensation system that reduces the small instrument flexure to negligible proportions. Long-exposure images on the sky show FWHM spot diameters of $34 \mu\text{m}$ ($0''.34$) averaged over the entire field of view. These are the best non-adaptive optics images taken in the visible at Keck Observatory to date. Maximum efficiencies are measured to be 28% for the echelle mode and greater than 41% for low-dispersion prismatic mode including atmospheric, telescope, and detector losses. In this paper, we describe the instrument and its development. We also discuss the performance testing and some observational results.

1. OVERVIEW

The Echelle Spectrograph and Imager (ESI) is a recently commissioned instrument available for use at the Keck II telescope of the W. M. Keck Observatory. ESI was built by the Instrument Development Laboratory of UCO/Lick Observatory at the University of California, Santa Cruz. The ESI instrument has three modes. The 160 mm diameter collimated beam can be sent directly into the camera for direct imaging through a prism disperser for low-resolution spectroscopy or to an echelle grating with prism cross-dispersion for moderate-resolution, large-wavelength-coverage spectroscopy.

An all-refracting 10 element all-spherical camera and a single ($2\text{K} \times 4\text{K} \times 15 \mu\text{m}$) CCD detector are used without modification for all three modes. The direct-imaging mode has a ($2'.0 \times 8'.0$) field of view (FOV) with $0''.15$ pixels. The low-dispersion prism-only mode (LDP) has a reciprocal dispersion of $50\text{--}300 \text{ km s}^{-1} \text{ pixel}^{-1}$, depending on wavelength. This mode can be used with an $8'.0$ long slit or in a multislit mode with user-made slit masks. The higher dispersion echelle mode gives the entire spectrum from 0.39 to $1.09 \mu\text{m}$ with a $20'.0$ slit length, in a single exposure. The reciprocal dispersion in echelle mode varies from 9.6 to $12.8 \text{ km s}^{-1} \text{ pixel}^{-1}$. Three five-bay filter wheels provide locations for up to eight different full-field filters, three multiobject slit masks, and the standard

complement of five echelle slits in a single bay. Each wheel also contains a single open bay.

The instrument was delivered to Keck II in 1999 July and saw first light on 1999 August 29. In its first 2 years of operation it has been scheduled for an average of 111 nights per year with instrument-reliability losses accounting for less than 2% of this time. In the imaging mode, ESI routinely delivers remarkable image quality. Long exposures with FWHM values less than $0''.45$ have been commonly obtained.

The Principal Investigator (PI) of the project was Joe Miller, director of Lick Observatory. ESI also had three Co-PIs: Michael Bolte, Puragra Guhathakurta, and Dennis Zaritsky. The optical designers were Brian Sutin and Harland Epps. David Cowley was the project manager. Initially (1995 November to 1997 July), Bruce Bigelow was the project scientist. After Bigelow left for Carnegie Observatory and for the remainder of the project, the project scientist responsibilities were split between project engineers Matt Radovan and Andrew Sheinis.

The principal niche envisioned for ESI was very high throughput moderate-resolution optical spectroscopy with wide wavelength coverage in a single exposure. Examples of the science programs that drove the choice of resolution are kinematic and abundance studies of distance galaxies, detailed abundance determinations for stars as faint as $V = 22$ (which includes the bright giants in Local Group galaxies), and absorption-line studies along the lines of sight to quasi-stellar objects. The low-dispersion/multiobject and direct-imaging capabilities were added after the echelle design was conceptualized. In the low-dispersion mode, ESI is likely the most powerful spectrograph in operation for obtaining low-resolution spectra of extremely faint objects. Redshift determinations and spectral energy distribution measurements for very faint

¹ UCO/Lick Observatory, University of California, Santa Cruz, Interdisciplinary Science Building, Santa Cruz, CA 95064; sheinis@ucolick.org, bolte@ucolick.org, epps@ucolick.org, kibrick@ucolick.org, miller@ucolick.org, mvr@ucolick.org.

² Carnegie Observatories, 813 Santa Barbara Street, Pasadena, CA 91101; bigelow@ociw.edu, sutin@ociw.edu.

galaxies or low-luminosity stars in the Galaxy are possible to $V \approx 25$. Examples of first-light science can be seen in Becker et al. (2000) and Prochaska, Gawiser, & Wolfe (2001).

This paper serves as a comprehensive overview of the instrument. For details about the individual subsystems, the reader is directed to the other articles in the literature describing various aspects of ESI: Kibrick et al. (2000), Sheinis et al. (1999a, 1999b, 2000), Sheinis, Nelson, & Radovan (1998), Radovan et al. (1998), Epps (1998), Epps & Miller (1998), Sutin (1997), and Bigelow & Nelson (1998). For observers planning to use ESI, the Keck Observatory WWW site for the instrument contains detailed specifications and descriptions of operational procedures.³

The wavelength range for ESI was chosen to lie between $0.39 \mu\text{m}$, where the best glasses for the visual range become acceptably transparent, and $1.1 \mu\text{m}$, where the efficiency of silicon CCD detectors approaches zero. The FOV imaged by ESI is a rectangle located $5'0$ off-axis from the telescope axis. It is $2'0$ wide in the radial direction by $8'0$ long. With this FOV, an on-axis (nearly) parabolic collimator imaging an off-axis field was required to minimize off-axis aberrations. The 2286.0 mm focal length of the collimator was chosen to be the longest that would fit into the Cassegrain module envelope, giving a 160.0 mm diameter beam. After the collimator, the optical elements used in the instrument are two flat fold mirrors, two prisms, a grating, the camera and shutter assembly, and the Dewar.

The requirements for the spectrograph optical layout are as follows:

1. The echellette spectral format must fill the CCD chip efficiently.
2. The orders must not overlap when a $20'0$ slit is used.
3. The individual slit images must be quasi-parallel over the entire detector.
4. The incoming beams should have minimum vignetting at the camera mouth.

1.1. Mode 1: Echellette in Near-Littrow Configuration

The primary mode of the spectrograph uses a catalog echellette grating (Spectronics $204 \times 204 \text{ mm}$, $175 \text{ lines mm}^{-1}$, $32'3$ blaze angle) to achieve a spectral resolution of 13,000 at the minimum 2 pixel slit width = $0'3$. This mode disperses the light from the $20'0$ slit into 10 orders, from order 6 in the red to order 15 in the blue. The minimum order separation is $22'0$. Table 1 shows diffraction orders, wavelength ranges, reciprocal dispersions, and rms image diameters for the echellette mode. The rms image diameters were calculated as a function of wavelength for all of the echellette orders. The calculation includes aberrations from the entire optical train. The diameters were calculated by apodizing the irregularly shaped Keck II primary mirror and by assuming perfect seeing.

TABLE 1
PREDICTED PERFORMANCE, ECHELLETTE MODE

ORDER	RANGE (μm)	D_{rms} (μm)	D_{rms} (arcsec)	IMAGING SCALE	
				\AA pixel^{-1}	arcsec pixel $^{-1}$
15	0.393–0.419	12.01	0.122	0.15	0.127
14	0.420–0.451	16.03	0.163	0.17	0.133
13	0.451–0.486	19.58	0.199	0.18	0.141
12	0.487–0.529	19.15	0.195	0.19	0.148
11	0.529–0.581	17.20	0.175	0.21	0.153
10	0.581–0.640	17.86	0.182	0.23	0.159
9	0.640–0.715	22.24	0.226	0.26	0.164
8	0.715–0.813	25.46	0.259	0.29	0.171
7	0.813–0.937	24.19	0.246	0.33	0.177
6	0.937–1.093	15.93	0.162	0.39	0.183

Figure 1 shows the physical layout of the spectrograph in echellette mode. The collimated light from the slit is pre-cross-dispersed by the first prism before it reaches the echellette grating, which is used nearly in Littrow for high efficiency. Although the spectrograph was designed specifically for this grating, other gratings could be manually installed. The grating-dispersed light is once again cross-dispersed by a second pass through the aforementioned prism. It then passes through the second prism before being imaged onto the detector by the underfilled $f/1.07$ camera.

Figure 2 shows an unprocessed echellette spectrum of a reference star. The entire spectral range from 0.39 to $1.09 \mu\text{m}$ is imaged without gaps. Orders run from 6 at the top to 15 at the bottom with red to the right. Note the two significant cosmetic defects in the lower right quadrant. A glowing pixel at row 85 of column 3895 contaminates a (10×10) pixel area, while 18 adjacent bad rows on the rightmost third of the device affect order 14 from 4460 to 4565 \AA . However, those wavelengths are available outside of the free spectral range in order 13.

The echellette orders are curved primarily by the anamorphic distortion in the prisms. They show a reasonably constant wavelength solution as a function of slit height. These wavelength solutions were used to calculate the residual tilts of the slit images. These tilts range from 0.8 ± 0.2 in order 6 to -1.3 ± 0.7 in order 15. Detailed plots of slit tilt with wavelength are available in Sutin (1997).

Figure 3 shows the reciprocal dispersion as a function of wavelength for each order in the echellette mode. The average reciprocal dispersion is about $11.4 \text{ km s}^{-1} \text{ pixel}^{-1}$.

1.2. Mode 2: High-Efficiency, Low-Dispersion Configuration

The high-efficiency, low-dispersion mode is achieved by modifying the optical path in the echellette mode (Fig. 1). This is done by inserting a flat silvered mirror in front of the echellette grating such that the beam will bypass the grating and be dispersed exclusively by the two prisms. The slit direction is then rotated by 90° to accommodate the new dispersion direction. The main strength of this mode is the high throughput,

³ See <http://www2.keck.hawaii.edu:3636/realpublic/inst/esi/esi.html>.

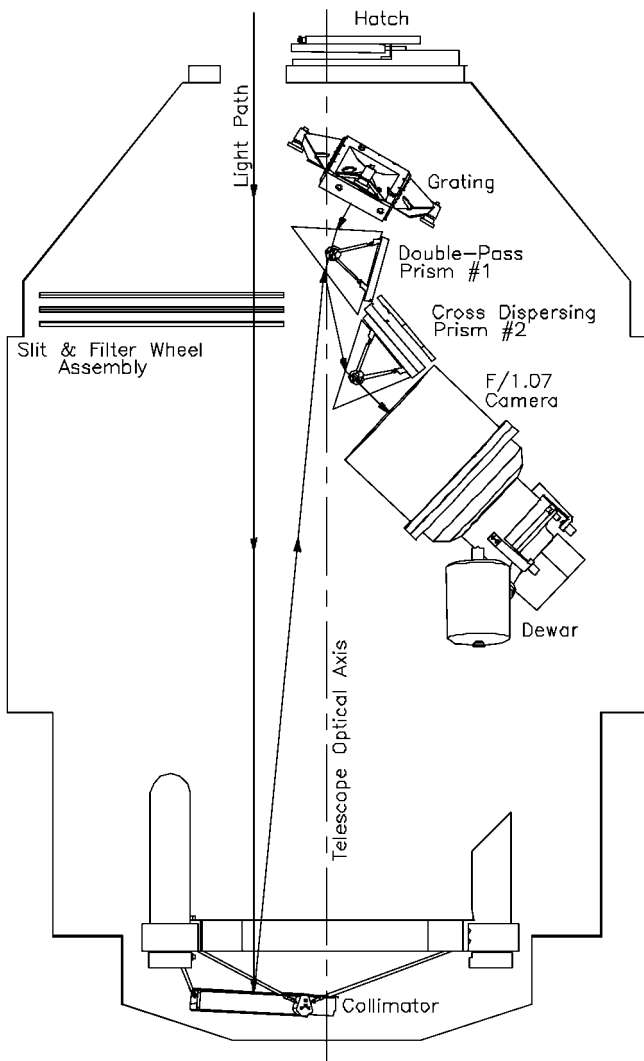


FIG. 1.—Schematic layout of echellette mode. This figure shows the physical layout of the spectrograph in echellette mode. The collimated light from the slit is pre-cross-dispersed by the first prism before it reaches the echellette grating, which is used nearly in Littrow for high efficiency. The grating-dispersed light is once again cross-dispersed by a second pass through the first prism and then passes through the second prism before being imaged onto the detector by the camera.

as the silvered mirror has higher efficiency than the aluminized grating.

Since the exit pupil of the collimator is near the prisms, FOV in this mode is not significantly restricted by vignetting at the prisms. Thus, an 8'0 long slit may be used. This maximum slit length is where the images begin to get “soft.” With a field this long, up to 50 slitlets could be cut into a slit mask within the 2'0 × 8'0 viewing area.

Figure 4 shows the spectrum of a reference star taken in this mode with ESI. This image has been processed using the Interactive Data Language (IDL) so as to align the apparent dispersion direction approximately with a single row. Note the curved sky lines due to the prismatic anamorphic distortion.

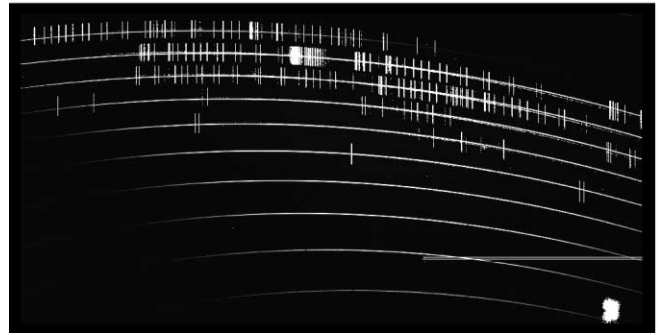


FIG. 2.—Unprocessed echellette spectrum of a reference star. Note the strong night-sky emission lines. The entire spectral range from 0.39 to 1.09 μm is imaged without gaps. Orders run from 6 at the top to 15 at the bottom with red to the right. Note the two significant cosmetic defects in the lower right quadrant. A glowing pixel at row 85 of column 3895 contaminates a 10×10 pixel area, while 18 adjacent bad rows on the rightmost third of the device affect order 14 from 4460 to 4565 \AA . However, those wavelengths are available outside of the free spectral range in order 13. (Note that this image has been rotated 90° in software, hence the CCD serial register runs vertically along the left edge of this figure.)

1.3. Mode 3: Direct-Imaging Configuration

The direct-imaging mode is achieved by modifying the optical path in the echellette mode (Fig. 1). This is done by translating the large postdispersing prism out of the beam and replacing it with a flat silvered mirror such that the beam will bypass all the dispersing elements and be sent directly to the camera, producing a 2'0 × 8'0 FOV. The slit wheel is generally turned to the open position, while the standard filter options, Johnson (*B*), Johnson (*V*), Spinrad (*R*), Gunn (*I*), are available only in a 2'0 × 2'0 format. The third filter wheel is available for user-supplied filters up to the 2'0 × 8'0 format.

2. OPTOMECHANICAL SUBSYSTEMS

The design of ESI was divided into several natural optomechanical subsystems: namely, the collimator, the prisms, the optical flats including the grating, the camera assembly, the detector and controller, the slit and filter wheel assembly, the calibration system, and the guider assembly. We now briefly discuss each of those subsystems. References are listed for readers interested in more detail.

2.1. Collimator

ESI uses a novel collimator system design, which is pictured in Figure 5 and is actively articulated in piston, tip, and tilt to provide the focus and the flexure control for the instrument. The details of this system are described in Radovan et al. (1998). The collimator mirror is 580 mm in diameter to accommodate the 2'0 × 8'0 FOV. It has a focal length of 2286 mm. The range of focus was selected to be ± 25 mm, which gives out-of-focus star-image diameters of 2'4. The collimator mirror is optimally constrained by a space-frame structure. The flexure compensation is accomplished by applying calibrated

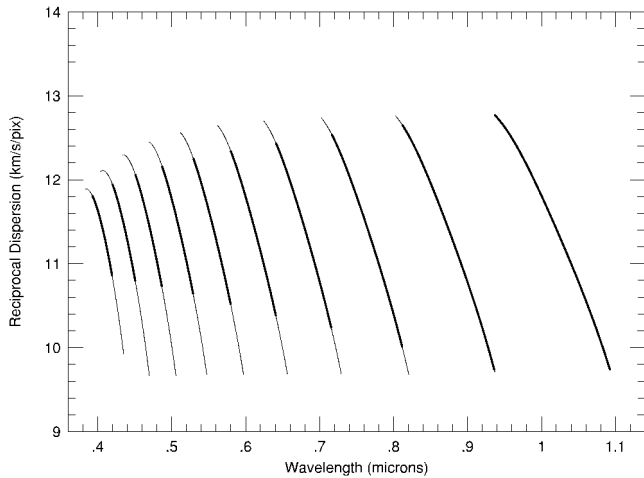


FIG. 3.—Reciprocal dispersion as a function of wavelength for each order in the echellette mode. The darkened portions of the curves show the free spectral range, while the lighter portions show the full extent of each order.

active correction for system gravity flexure in an open loop fashion to the collimator.

The flexural requirement for any 2 hr observation was that the spectra should remain stable on the detector to within $\pm 0''.04$ (peak to valley) with (open loop) flexure compensation. At the final imaging scale of $0''.153 \text{ pixel}^{-1}$, this requirement corresponds to $\pm \frac{1}{4}$ pixel. In order to achieve the required flexure compensation precision, collimator tilt increments must be controlled in $0''.01$ units upon the sky, corresponding to collimator tilts of $0''.327$. With actuator separations of 1200 mm, that corresponds to actuator motions of $1.65 \mu\text{m}$. In order to achieve the desired correction precision, hysteresis and slip levels were maintained below this value.

2.2. Cross-Dispersion Prisms

ESI uses two large (25 kg), 50° angle prisms for cross-dispersion. The optical requirements for the prisms were high transmission, small index inhomogeneity, and a large ratio of red dispersion relative to blue dispersion while maintaining as high an index as possible. Fused silica was considered; however, its relatively low index would have required 55° prisms, which would have complicated the optical and coating designs. Ohara BSL7Y was selected for the prisms, as its optical properties provide an optimal combination of the requirements listed above.

Various index-inhomogeneity models for the prisms were computed and ray-traced. The results of this modeling suggested that the index homogeneity must be constant to approximately $\pm 10^{-5}$. Our contract with the vendor did not guarantee this level of precision. However, we were able to request fabrication on a “best effort” basis. Interferograms of the finished prisms taken in transmission, along with the final

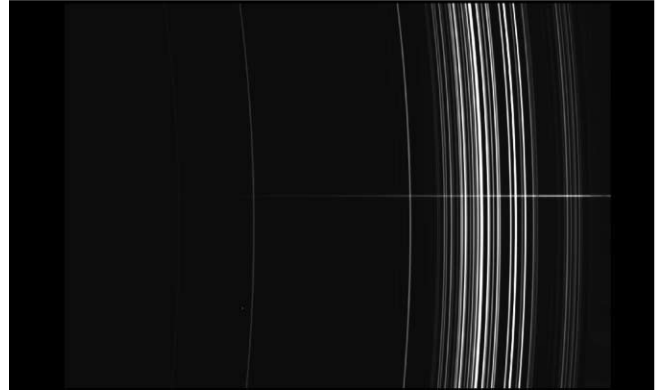


FIG. 4.—Spectrum of a reference star taken in the high-efficiency, low-dispersion mode with ESI. This image has been rotated with software so as to align the apparent dispersion direction approximately along the detector row direction. Note the curved sky lines due to the prismatic anamorphic distortion.

image quality tests, show that the fabricated prisms are homogeneous to approximately $\pm 2 \times 10^{-6}$.

The prisms are mounted within the spectrograph using determinate structures. These structures are extremely rigid for their weight because mount material is used in compression or tension only. The mounts are designed such that no moments can be imparted at the mount-to-glass interfaces, thereby ensuring that the glass is isolated from any mechanical stresses developed inside the instrument structure. The prisms and their associated mounting mechanisms are described in Sheinis et al. (1998).

2.3. Kinematic Mirror Mechanisms

ESI uses two moderate-weight (10 kg) translating fold mirrors to switch between modes. The scientific requirements for the spectrograph are such that the spectra may move by no more than $\pm 0''.04$ on the sky ($\frac{1}{4}$ pixel) in switching between modes and back again, so as to accommodate the use of a single set of standard reference spectra and flat-field data between different exposures. This places a $\pm 1''.3$ allowable tip and tilt repeatability on the mirrors. A novel locating mechanism design was developed to achieve the repeatability needed for these mirrors. This mechanism is described in detail in Sheinis et al. (1999a).

2.4. Camera Subsystem

The camera optical design is shown in Figure 6. It consists of 10 lens elements in five lens groups. The camera has an effective focal length of 308 mm. It has an entrance aperture diameter of 287 mm and a final plate scale of $97.7 \mu\text{m arcsec}^{-1}$ on the sky. The collimated beam diameter is approximately 160 mm. The camera’s effective f /ratio in imaging mode is thus $f/1.93$ and slightly faster in spectroscopic modes as a result of anamorphism.

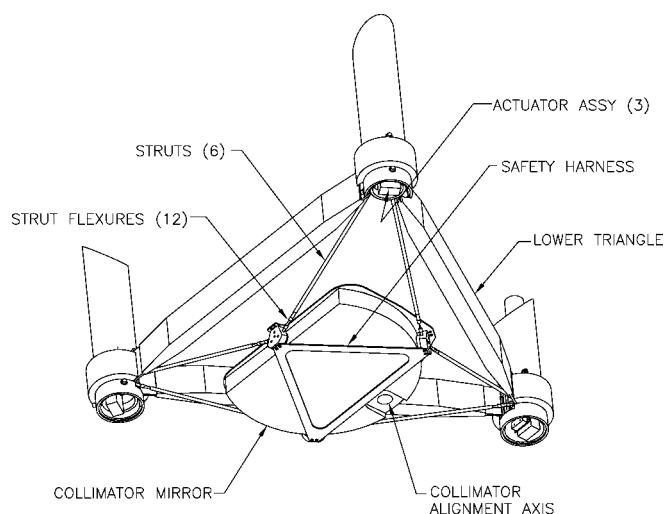


FIG. 5.—ESI collimator system design, which is actively articulated in piston, tip, and tilt to provide the focus and the flexure control for the instrument. The collimator mirror is 580 mm in diameter with a focal length of 2286 mm.

The camera design is all-spherical, and it includes three large CaF_2 lenses. Group 1 is a doublet, group 2 is a CaF_2 singlet, groups 3 and 4 are triplets, while group 5 is the field flattener/Dewar window. The elements in groups 1 and 3 are optically coupled with a fluid (Cargille laser liquid type 5610 $n_D = 1.5000$) to minimize internal reflections. The elements in group 4 are greased together with Dow Corning Q2-3067 optical couplant. The six larger elements were fabricated by TORC (Tucson, AZ), and the four smaller elements were fabricated by Cosmo Optics, Inc., (Middletown, NY). Broad-passband antireflection coatings were applied by Coherent Auburn Division (Auburn, CA).

The ESI optical design is complicated by the fact that a wide variety of pupil anamorphic factors and effective entrance pupil distances is presented to the camera's entrance aperture by the three operating modes. (In practice, the camera design was slightly compromised in the imaging and LDP modes so as to favor the echellette mode.) Nevertheless, the echellette mode remains the most severe test of system image quality.

In order to produce detailed sensitivity analysis, individual lens elements were perturbed axially, radially, and in tip/tilt within the computer model. The perturbed camera model was ray-traced within the ESI spectrograph numerical model in echellette mode at 50 different wavelengths, covering all 10 orders. The perturbed system was compared to the unperturbed system in order to determine the sensitivity coefficients of the camera. The worst centroid location change and worst increase in the rms spot-size diameter (D_{rms}) were noted. A similar analysis was performed for the lens groups. After moving entire groups, we calculated the resulting centroid motion and change in D_{rms} .

These sensitivities were used to estimate manufacturing and assembly tolerances for the mechanical components such that

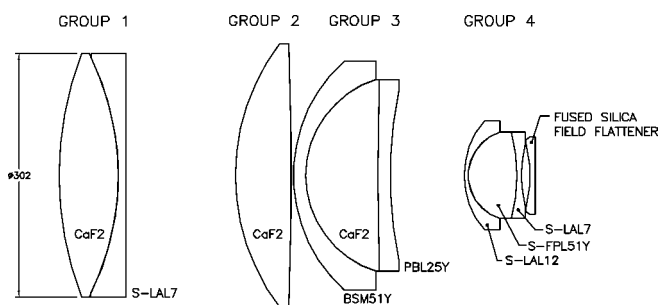


FIG. 6.—ESI camera design is all-spherical, and it includes three large CaF_2 lenses. The elements in groups 1 and 3 are optically coupled with a fluid (Cargille laser liquid type 5610 $n_D = 1.5000$) to minimize internal reflections. The elements in group 4 are greased together with Dow Corning Q2-3067 optical couplant.

the expected summation of image errors (added in quadrature) was comparable to the residual aberrations in the optical design. In addition, the sensitivity data allowed setting of a lens-motion tolerance in terms of the total allowable image motion for the different gravity orientations.

2.4.1. Camera Optomechanical Design

The camera mechanical system (CMS) for ESI was designed by J. Alan Schier Co. (La Crescenta, CA) and fabricated by Danco Machine, DPMS, Inc. (Santa Clara, CA). The CMS is shown in Figure 7. It consists of four cells supported within a single large barrel. The mass of the entire camera assembly, consisting of the CMS and the lens elements, is approximately 125 kg. The individual cells with their respective lens elements have masses ranging from 5 to 30 kg. The cells locate radially against locating surfaces (lands) on the barrel inner wall and axially against athermalizing spacers. Each cell consists of an aluminum housing, radial athermalizing spacers, and a compressive preload spring. Each of the two oil-coupled cells also contains an oil-sealing and oil-reservoir system. The lens element spacings within the oil-coupled cells are maintained by 0.10 mm Mylar spacers, placed between the lens elements at their edges.

To accommodate the optical coupling fluid, cells 1 and 3 contain an O-ring seal at each glass-aluminum interface. The O-rings are compressed to the minimum nominal dynamic seal specification (8%). The O-rings are compressed such that the optic locates directly against the aluminum land and the O-ring carries most of the load while providing a seal.

A polyurethane bladder is used to accommodate volumetric changes of the coupling fluid within each cell. Possible reactivity of the optical coupling fluid with polyurethane and other substances was tested by Hilyard, Laopodis, & Faber (1999). They found no reactivity with the polyurethane bladder material.

The major features of the optomechanical design and the assembly of the camera are detailed in Sheinis et al. (1999b).

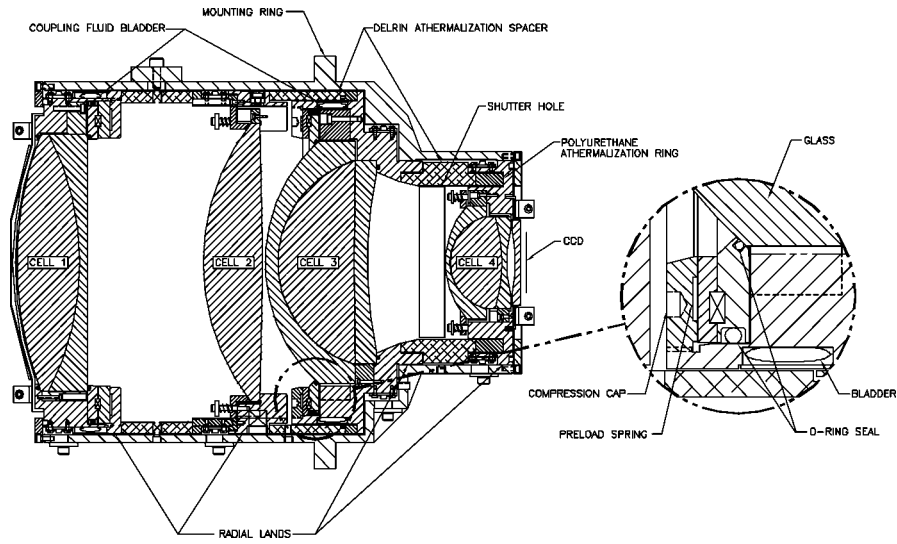


FIG. 7.—Camera mechanical system (CMS) consists of four cells supported within a single large barrel. The cells locate radially against locating surfaces (lands) on the barrel inner wall and axially against athermalizing spacers. Each cell consists of an aluminum housing, radial athermalizing spacers, and a compressive preload spring. Each of the two oil-coupled cells also contains an oil-sealing and oil-reservoir system.

2.4.2. Camera Bench Testing and Performance Analysis

After assembly of the camera, numerous optical performance tests including interferometric testing, polychromatic point-spread function measurements, and back-focal-distance measurements were carried out. The results of these tests compared well with the predictions from the lens design. For example, the polychromatic (Wratten 54) rms spot diameter on-axis was measured to be 13.7 μm , as compared to a predicted rms spot diameter of 12.5 μm . These tests are discussed in detail in Sheinis et al. (1999b).

2.5. Detector and Controller

The ESI detector (device W62C2) is an MIT/Lincoln Labs CCID20 high-resistivity CCD. For details, see Burke et al. (2000). It uses readout amplifiers at both ends of the serial register. Measured deviations from flatness are 18 μm peak to valley at the normal operating temperature of -120.0°C . At that temperature, the on-chip amplifier read noise as measured

in the laboratory is 2.3 electrons for one amplifier and 2.6 electrons for the other. When the CCD Dewar is mounted in ESI, the ESI instrument is mounted on the Keck II telescope, all of the motorized stages within ESI are powered up and operating, and the telescope is tracking, the measured readout noise for each amplifier increases by 0.3 electrons.

Operating at -120.0°C , the dark current is 2.1 electrons $\text{pixel}^{-1} \text{hr}^{-1}$ in non-multi-pinned phase (MPP) mode. At that temperature, the various wavelength-dependent specifications for the CCD are shown in Table 2. Note that these MIT/LL devices are not capable of MPP mode operation.

The CCD controller for ESI is a San Diego State University second-generation device (SDSU2) developed by Leach, Beale, & Eriksen (1998). It provides both a low-gain and a high-gain mode of operation. While the pixel full well of this CCD is 105,000 electrons, the achievable full well is limited by the 16 bit resolution of the analog-to-digital conversion. Table 3 shows the achievable full well as a function of the selected gain.

The controller also provides a software-selectable choice of three different readout speeds. However, nearly all observations are performed using the fastest of the three speeds. Table 4 provides the details of the per-pixel timing for the fastest and slowest speeds, while Table 5 shows the serial charge transfer efficiency (CTE) for this CCD as a function of the selected

TABLE 2
CCD QUANTUM EFFICIENCY AND FRINGING

Wavelength (\AA)	Quantum Efficiency (%)	Fringing (%)
3200	10.2	
4000	60.8	
5000	82.4	
6000	80.3	
7000	77.1	
8000	68.9	12.0
9000	45.0	15.0
10000	11.3	30.0

TABLE 3
ACHIEVABLE FULL WELL VERSUS GAIN

Mode	Gain ($e^- \text{DN}^{-1}$)	Achievable (e^-)	Percent of Pixel Full Well
Low gain	1.30	84,500	80
High gain	0.52	31,000	30

TABLE 4
PER-PIXEL TIMING VERSUS READOUT SPEED

Readout Mode	Sampling Time (Baseline + Video) ($\mu\text{s} + \mu\text{s}$)	Serial Width (μs)	Pixel Overlap (μs)	Pixel Period (μs)	Pixel Frequency per Amplifier (Kpixels s^{-1})
Fast	1 + 1	3	1	7.2	139
Slow	5 + 5	17	7	25.2	40

NOTE.—Serial transfer is overlapped with video processing.

readout speed. Note that the parallel CTE for this device is 0.9999999 (virtually perfect) at -120.0°C for all readout speeds and that the readout noise is the same at all readout speeds. While the slow-speed readout mode is seldom used, it does provide for nearly perfect serial CTE at the cost of significantly increased readout time.

The controller provides software selection of single-amplifier mode readout from either of the two on-chip amplifiers, or dual-amplifier readout using both amplifiers. In normal operation, dual-amplifier readout is used. Table 6 provides the readout times for various operating modes.

While the controller supports both horizontal and vertical on-chip binning, it should be noted that on these MIT/LL CCDs, the full-well capacity of the pixels in the serial register and in the summing well is not significantly larger than the full well of the pixels in the imaging area. Unfortunately, the limited well depth of the serial register pixels and the summing well significantly constrain the exposure levels that can be utilized when using on-chip binning.

2.5.1. CCD Dewar

The Dewar holds approximately 4 liters of liquid nitrogen, which is available to cool the CCD to -120.0°C . The hold time for the half-full vessel is approximately 20 hr. The CCD is supported in the Dewar housing by a hexapod structure. This structure provides a very rigid support and thermal standoff for the CCD. The flexure of the cryogenic container is isolated from the CCD by a flexible copper braid that connects the chip to the cold finger. The vacuum housing with cyro-container is kinematically mounted to the back flange of the camera. The kinematic mount has three adjustable screws to tip, tilt, and piston the CCD for alignment to the focal plane. The Dewar can be removed from the camera and reattached to the kinematic mount without disturbing the Dewar alignment. The alignment of the spectra on the chip is also adjustable by means of a cam that rotates the Dewar about the optical axis. Like the piston and tip/tilt adjustment, this is a one-time-only adjustment that is preserved if the Dewar is removed.

2.6. TV Guider

The guider system design is pictured in Figure 8. The guider system combines a 200 mm Canon lens, a Photometrics PXL camera with a $1\text{K} \times 1\text{K}$ ($24 \mu\text{m}$ pixels) detector, and a Melles

TABLE 5
SERIAL CTE VERSUS READOUT MODE

Readout Mode	Per-Pixel Time ($\mu\text{s pixel}^{-1}$)	CTE	Loss after 1024 Transfer (%)
Fast	7.2	0.99998	2.0
Normal	10.5	0.99998	2.0
Slow	25.2	0.999996	0.4

NOTE.—Serial transfer is overlapped with video processing.

Griot shutter to produce a $4'0 \times 4'0$ FOV on the sky. The guider FOV includes a $1'5 \times 4'0$ portion of the instrument FOV, with the remainder of the guider field being located on a fixed mirror adjacent to the slit masks. The guider system also has an eight-position filter that can accommodate 50 mm^2 filters (1–10 mm thicknesses).

In addition to the FOV requirements and the functional requirements (which included the provision of a remotely controlled focus and filter wheel assembly), the TV system needed to meet a strict flexure specification. This was because the system guides by centroiding on an offset image. Because of mechanical constraints imposed by the position of the spectrograph optics, the chosen guider field is more off-axis than the scientific field. The echellette slit plate is tilted away from the focal surface so as to allow the TV-guider system to be moved out of the incoming beam while leaving the entire slit plate within the depth of focus of the spectrograph. This configuration requires that the guide stars in the TV mirror do not come to focus on the surface of the mirror. Therefore, they cannot benefit from reference marks on the mirror surface. For this configuration, any flexure in the TV system optical path will introduce a gravity-dependent error in the telescope pointing.

2.7. Calibration Source

Each of the two ESI calibration systems consists of one or more source lamps, condensing/relay optics, a fiber-optic light guide, a projecting optic, and a diffusing panel common to both systems. The first system contains lamps for neon, argon, mercury-neon, and a quartz-continuum source. The second contains a low-pressure copper-argon line lamp. Both systems may be used simultaneously, which allows for independent selection of any combination of source lamps. The lamps are physically separated and thermally isolated from the pri-

TABLE 6
READOUT TIMES FOR FULL CHIP

Amplifier Mode	Fast Readout (s)	Slow Readout (s)	Binning
Dual amplifier	39	128	None
Single amplifier	70	240	None
Dual amplifier	23	67	2×2
Single amplifier	38	122	2×2

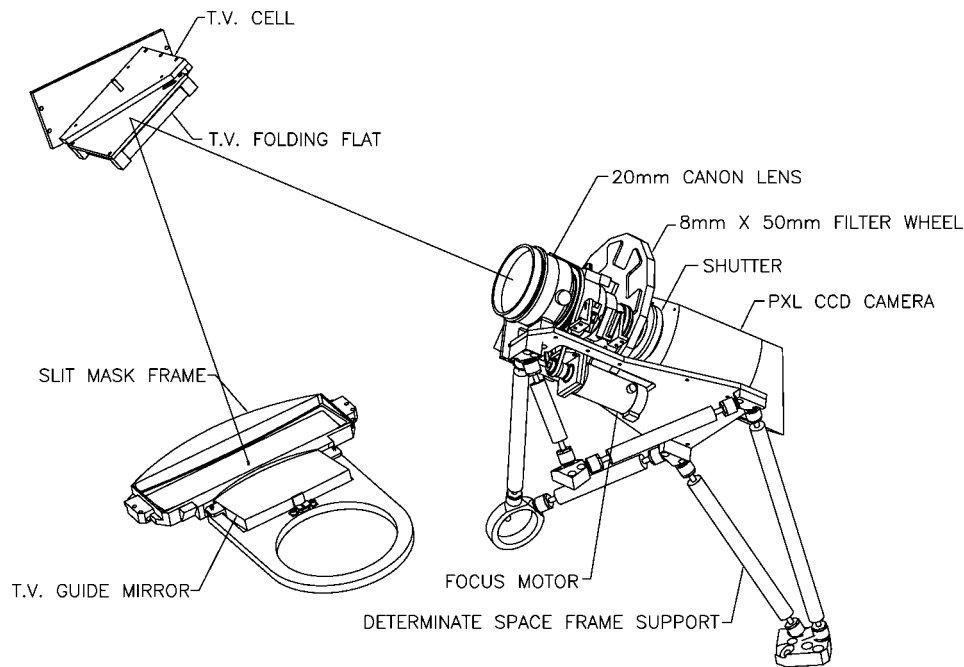


FIG. 8.—ESI guider system: combines a 200 mm Canon lens, a Photometrics PXL camera with a $1\text{K} \times 1\text{K}$ ($24\ \mu\text{m}$ pixels) detector, and a Melles Griot shutter to produce a $4'0 \times 4'0$ FOV on the sky.

mary optical path of the spectrograph in order to limit internal lamp-induced seeing. The fiber-optic light guide delivers light of appropriate wavelengths to a diffusive reflecting panel located on the back of the spectrograph entrance hatch. The light is then relayed through the spectrograph to the CCD.

3. STRUCTURE

3.1. Requirements

The design of the ESI instrument structure was constrained by weight, center of gravity, volume, and stiffness requirements, as well as budget and schedule considerations. Cassegrain-mounted instruments for Keck must attach to an instrument module, which serves as a carriage for loading the instrument on the telescope and as a storage cart when the instrument is not in use. The Cassegrain module also provides a bearing for field derotation as well as mechanical, electronic, and data interfaces between the telescope and the instrument.

The external requirements for the instrument include (1) a mass limit of 2425 kg for the instrument+module unit; (2) the instrument+module center of gravity must be located *at the center* of the Cassegrain module rotation bearing; and (3) the instrument must stay within a space envelope that is roughly cylindrical in shape, 2.0 m in diameter, and 2.5 m long.

The structural stiffness requirements are crucial to the performance of the instrument. A detailed sensitivity analysis of image size and motion, as functions of translations and rotations of the individual optical components, was used to set the allowable deflections and rotations in the structure. The dynamic

response of the structure (first resonant frequency) was assigned a minimum value of 30 Hz.

Based on experience with the Keck Low-Resolution Imaging Spectrograph (LRIS; Oke et al. 1994), it was known that significant deformations of the Cassegrain module and rotator bearing were due to forces passed through the module mounting points by deflection of the Keck primary mirror cell. Given the overconstrained connection between the telescope and module, the decision was made to use a determinate space frame for the ESI instrument structure and to attach it kinematically to the Cassegrain module. This determinate space frame isolates the optical structures in the instrument from almost all the torques introduced by the bearing. In keeping with the instrument budget and schedule constraints, steel was chosen as the frame material.

3.2. Structure Overview

The center of the ESI structure is a triangular mainframe, which provides the foundation for the substructures and the connections to the rotator bearing. Extending below the mainframe is the collimator structure, which supports the tip/tilt and piston actuators carrying the collimator mirror. Details of the support and drive of the collimator mirror flexure control are described in § 4. The optics support structure (OSS) and the slit area stages are located above the mainframe. The OSS is mounted to the mainframe via a determinate structure. The slit area stages are mounted via an overdetermined structure. After preliminary conceptual designs for the structure and links were

completed, finite-element modeling, using the ANSYS program, was used to examine the static and dynamic response of the structure.

The primary concern about the static response of the structure was to maintain the global tilts of the collimator below the allowable values prescribed by the error budget. Hence, analyses were carried out for the three orthogonal gravity orientations (X , Y , and Z). Tilts of the plane containing the three-collimator support point were calculated from the resulting structural deflections. The worst-case tilts of the collimator-support triangle were well within the error-budget specification. Peak deflections of the collimator mounting points occurred with gravity parallel to the optic axis and had a peak value of $136\ \mu\text{m}$. The deflections in this orientation corresponded to an “unscrewing” of the structure relative to the mounting points on the rotator bearing. These deflections had little effect on the optical performance, as the motion of the collimator is primarily rotation about its parent axis.

The primary goal for the dynamic response of the structure was that its first resonance be significantly higher than the lowest resonant frequencies in the telescope structure, which are of the order of 10 Hz. As mentioned above, the maximum static deflection in the structure was calculated to be $136\ \mu\text{m}$. Assuming the well-known spring-mass equivalent system, the first resonant frequency of the structure can be calculated directly from this deflection. This first resonant frequency was 42 Hz, well above that for the telescope.

3.3. Optical Substructure

The OSS was designed as a bolted box to which the grating, fixed prism, moving prism, imaging mirror, low-dispersion mirror, and the camera attach. The decision to use this approach rather than a pure space-frame approach was driven by the complications imposed by a three-mode instrument. The large moving masses (prism and two mirror assemblies) coupled with the tightly packaged and folded optical path made the box solution very appealing. All optical assemblies were designed to attach to the OSS in quasi-kinematic ways to ensure that deformations of the box (OSS) would cause only free-body motion of the subassemblies rather than deformations. Two methods of attachment were used, depending on the optic.

The two fixed optics, one prism, and the camera were attached to the OSS by hexapods. The connection points (nodes) were chosen to be at the intersection of three plates so that reaction force in the OSS structure could be provided by the vector sum of shear forces in the plates. Stated in different terms, the OSS was designed in a manner that ensured that the plates could not react in any bending mode.

The OSS's main performance requirement was the instrument flexure specification. Because it held all spectrograph optics except the collimator, any differential rotation of the OSS's optical axis relative to the collimator would result in large image motion at the CCD. To complicate matters, this

assembly is very massive, and it produces the largest component of the instrument flexure. Thus, the most significant reduction in total flexure was accomplished by minimizing the OSS flexure. For this reason, a hexapod structure was used to attach the OSS to the mainframe. In addition to its inherent large stiffness, the hexapod structure also provided an easily alignable support for the OSS.

3.4. Filter and Slit Wheels

ESI uses a triple-wheel filter/slit assembly located near the Cassegrain focus to hold a variety of removable slit and filter components. Each wheel has five bays that can accommodate as many as three 2.0×2.0 filters each. Only the topmost wheel is at the telescope focus. It can hold as many as four different long-slit and/or multislit plates, as well as the full complement of echellette slits. In practice, one bay is left empty to allow for direct imaging. Each wheel of the triple-wheel assembly consists of a DC gear motor mechanically coupled to an optical encoder system and a metal-belt-driven wheel with a second optical encoder to provide a dual-closed-loop control system for angular wheel positioning.

4. FLEXURE MINIMIZATION

The predicted mechanical performance of ESI is based on the combination of a detailed set of optical sensitivities from the optical design analysis and a finite-element analysis of a slightly simplified structure model.

The flexure compensation system is a passive mathematical representation of previously observed image motions, used to predict the expected image position for any altitude and azimuth location of the telescope. The flexure compensation is provided open loop by actively tilting the collimator mirror, so as to compensate for the combined motions of all the other optics in the optical train. We report on the details of this modeling and the results of the flexure testing in the laboratory and at the telescope with and without flexure compensation.

4.1. Passive Flexure Performance

Because most of the structures of the instrument are determinant space frames, it is possible to model the instrument with a relatively simple finite-element model (FEM). The goal of this analysis was to use predicted motions of all the optical components as a function of gravitational orientation so as to predict the resulting image motion. To accomplish this task, we calculated the optical sensitivity of the final image location to motions of each optic individually in all 6 of its degrees of freedom. We then combined the FEM predictions of the optic motions for various gravity orientations with these signed sensitivities to get the resultant image motion at the detector for any orientation of ESI. This FEM was then used to optimize the structure for minimum image motion at the detector during the design process.

4.1.1. Requirements

The passive flexure goal was set at $\pm \frac{1}{2}$ pixel for any 2 hr observation. Predictions of the real-world performance of ESI based on the FEM and laboratory tests were not easily and directly compared to this specification. We modeled and measured flexure in an orthogonal coordinate system (altitude and instrument position angle), but transforming that into what one can reasonably expect during the worst-case observation would require searching through all possible 2 hr integration paths on the sky. This would need to be repeated *for every change in the FEM*. For simplicity, we chose to minimize the overall flexure with respect to our orthogonal coordinate system, rather than in terms of image trajectories on the sky (altitude and azimuth).

4.1.2. FEA Model

We used a finite-element analysis (FEA) model to predict the total image motion in a spectrograph as a function of the gravity vector. The philosophy we chose was to formulate a relatively simple macrostructure model of the instrument while doing our best to design optical mounts that had stiffness well beyond the expected stiffness of this instrument macrostructure. Performance of the optical mounts was analyzed analytically and with FEA, then optimized for flexure independently of the macrostructure. This allowed us to ignore the details of the optical mounts in the FEA macrostructure model. The predicted motion of each of the optics from the FEA was entered into a spreadsheet and multiplied by the signed image-motion sensitivities to predict the total effect of instrument flexure on instrument flexibility. These predictions were instrumental in locating and remedying several weaknesses in the design.

4.1.3. Analysis and Testing

To confirm the image motion predictions in the laboratory, ESI was assembled and installed into a test fixture that produced the variations in position angle and elevation that the instrument would see in the telescope. By iterating between the laboratory testing and the FEA modeling, we were able to identify and remedy one major and several minor problems that helped to reduce the instrument flexure to a final rms value (with active compensation on) of approximately ± 0.25 pixels in each mode for all orientations. The overall flexural performance is described in the next section.

4.2. Active Flexure Compensation

4.2.1. Overview

The ESI flexure compensation system (FCS) utilizes a mathematical model of gravitationally induced flexure to periodically compute and apply flexure corrections by commanding the corresponding tip and tilt motions to the collimator. For details, see Kibrick et al. (2000). Separate flexure models are

used for each of the three spectrograph modes (echellette, low dispersion, and imaging). Although the flexure model is recalculated at a 1 Hz rate, corrections are not applied until the accumulated image motion reaches 0.1 pixel in magnitude so as to avoid unnecessary use of the collimator actuators. All three actuators are updated in parallel to minimize response time and mechanical stress on the collimator mechanism.

The ESI FCS compensates only for those errors that can be modeled in terms of gravity-driven flexure. Nonmodeled errors include those that result from changes in temperature across the instrument structure, from lost motion in optical stages, and from small zero-point shifts that are observed whenever the instrument is removed from and then reinserted into the telescope. In addition, there is out-of-roundness or runout between the instrument and the rotator module. While the determinate structure that attaches ESI to the rotator module isolates most of the bearing stresses from the instrument, a small amount of residual stress contributes to the observed hysteresis and image motion. Image motions induced by such stresses are neither modeled nor corrected by our model of gravitationally induced flexure.

The first operational test of the FCS system took place during instrument commissioning at the Mauna Kea summit in 1999 September. The flexure model was refined during subsequent engineering runs in October and November. The system became operational for science observing at the end of 1999 and is now in routine use. Image motion due to flexure has been reduced from the uncompensated state by approximately a factor of 10 to a few tenths of a pixel (or about $0''.04$ on the sky) for a typical flexure-compensated exposure.

4.2.2. Modeling

Measurements of image motion versus collimator motion were obtained in all three instrument modes to determine the relevant transformations and to verify that the system operated linearly. The plate scale varies as a function of position on the detector as a result of the anamorphic distortion in the prisms. In order to simplify the control algorithm, a specific image feature near the center of the detector was selected as the central reference for each instrument mode. The gains (image motion vs. collimator tilt) for each actuator were then determined for each instrument mode using their respective reference features. These same reference features were later used when measuring the image motions induced by spectrograph flexure. These measurements were obtained with the instrument and rotator module installed in the Keck II telescope.

Given the space-frame structures used for ESI, a linear elasticity model of gravitational flexure was used for fitting the image motion versus spectrograph position data. The equations

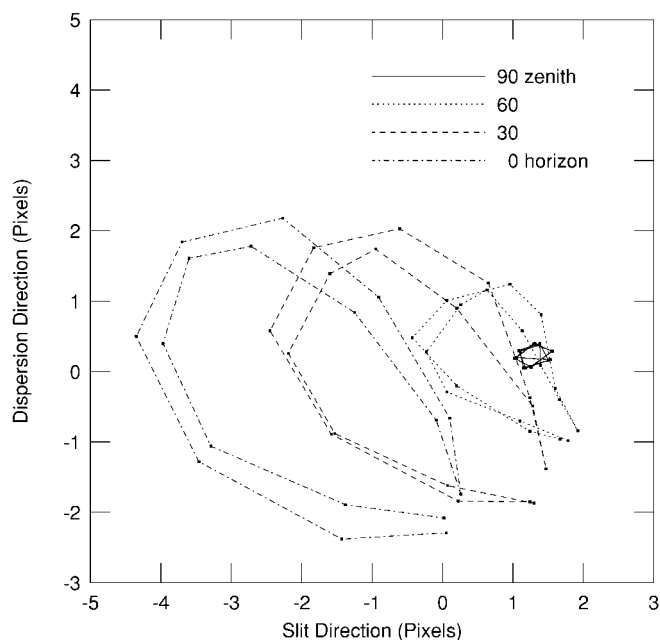


FIG. 9.—Echellette mode flexure measured in 1999 October with active flexure compensation system disabled. The telescope was stepped in elevation between 0° , 30° , 60° , and 90° . At each of these four elevations, calibration data were obtained at 17 different rotator position angles, sampling two full revolutions (one clockwise, one counterclockwise) in increments of 45° of rotation.

for this gravitational flexure model are as follows:

$$X(\phi, \theta) = a_0 + a_1 \cos \phi \cos \theta + a_2 \cos \phi \sin \theta + a_3 \sin \phi, \quad (1)$$

$$Y(\phi, \theta) = b_0 + b_1 \cos \phi \cos \theta + b_2 \cos \phi \sin \theta + b_3 \sin \phi, \quad (2)$$

where X corresponds to the predicted position of the reference feature in the X (or column) axis of the CCD, Y is the predicted position in the Y (row) axis, ϕ is the telescope elevation angle, θ is the rotator physical angle, and the a_i and b_i are the corresponding coefficients obtained from a least-squares fit of the data to the model. Each instrument mode is fitted separately.

The gravitational flexure model provided a relatively good fit to the observed data for all three modes. The worst-case residuals (vector magnitude of X and Y residuals) in each mode were imaging mode, 0.63 pixels; low-resolution mode, 0.66 pixels; and echellette mode, 0.64 pixels. The corresponding rms residual errors were imaging mode, 0.29 pixels; low-resolution mode, 0.25 pixels; and echellette mode, 0.25 pixels. These residuals are not unreasonable given the nonmodeled image motions observed at zenith plus the several tenths of a pixel hysteresis observed at all positions. Since 1 pixel cor-

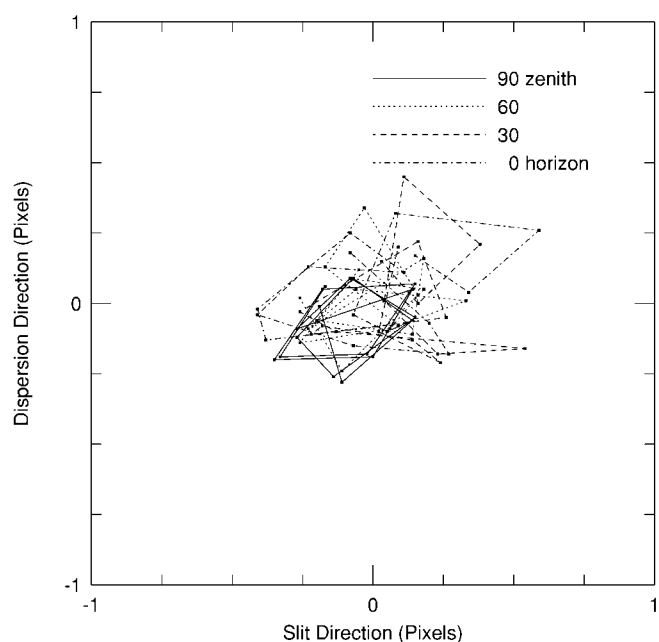


FIG. 10.—Echellette mode residual flexure measured in 1999 October with the active flexure compensation enabled. Data were collected in the same manner as described for Fig. 9.

responds to $0''.153$ on the sky, worst-case residuals were about $0''.1$ and rms residuals were about $0''.04$.

4.2.3. Initial Results

Measurements of image motion induced by spectrograph flexure were obtained with the instrument and rotator module installed in the Keck II telescope. Calibration spectra were obtained in the two spectroscopic modes by illuminating a pinhole adjacent to the echellette slit with the various line lamps. Images of this pinhole were also obtained in imaging mode. The telescope was stepped in elevation between 0° , 30° , 60° , and 90° . At each of these four elevations, calibration data were obtained at 17 different rotator position angles, sampling two full revolutions (one clockwise, one counterclockwise) in increments of 45° of rotation. All flexure measurements were made using the same central reference features for each mode as were used to calibrate the actuator gains.

The results of the flexure measurements obtained during the 1999 October engineering run are shown for the echellette mode in Figures 9 and 10. The results for the other two modes are similar. Note that in echellette mode the dispersion direction is parallel to the columns (or Y -axis).

4.2.4. Long-Term Results

The long-term stability of the FCS calibration has been measured by comparing the echellette mode flexure models that were derived from flexure calibrations performed in 1999 Oc-

tober and November with those obtained from a pair of calibrations conducted on the same night in 2001 March. While some large zero-point shifts (the a_0 and b_0 terms) were observed when comparing the 2001 calibrations to those performed in 1999 (see Table 7), these were most likely the result of an adjustment to the Dewar position performed in 2000 January. However, the zero-point stability over the course of one night is about 0.15 pixel. Thus, one can compensate for any longer term zero-point shifts by taking a single calibration exposure at the start of the night and adjusting the FCS operational zero point accordingly.

While the values of the angularly dependent model coefficients (a_1, a_2, a_3 and b_1, b_2, b_3) varied by as much as 20% from one calibration model to the next, the models they represent agree quite closely once the respective zero points are aligned. Predicted image positions from each of the four models produced by these calibrations were compared. The worst-case differences observed between corresponding positions were 0.43 pixel in X and 0.24 pixel in Y . The rms errors across positions predicted by all four models were 0.11 pixels in X and 0.07 pixel in Y .

On the basis of these results, and assuming that no significant mechanical or optical modifications are made to the instrument, a given flexure calibration model can be expected to provide acceptable FCS performance for at least 1 yr. Thus, aside from nightly checks of the FCS zero point, frequent recalibration of the flexure model is *not* needed to maintain FCS performance.

5. OPTICAL PERFORMANCE

In the following section, we report on the optical performance of the spectrograph. We compare predicted results from a detailed end-to-end optical model of the instrument to optical tests performed in the laboratory at Santa Cruz and on Mauna Kea, and on the sky.

5.1. Direct-Imaging and Spectral-Imaging Performance

5.1.1. Predicted System Performance

The system performance reported here was calculated using an in-house lens analysis code written by one of the authors

TABLE 8
MEDIAN RMS SPOT DIAMETERS

MODE	MEASURED		DESIGN	
	μm	arcsec	μm	arcsec
Echelle	31.7	0.32	19	0.19
LDP	30.8	0.31	16	0.16
Imaging	37.4	0.38	24	0.24

(B. S.). This code was used to model the entire spectrograph including the final as-built camera. Orders 6 in the infrared through 15 in the blue were ray traced at five wavelengths uniformly spaced over each free spectral range, without refocus. The rms spot-size diameter D_{rms} was calculated for each image. Averaging these image diameters over all wavelengths and all orders, the $\text{Ave}(\text{rms}) = 19.0 \pm 3.3 \mu\text{m}$. The corresponding 80% encircled ray diameter average is $\text{Ave}(80\%) = 22.5 \pm 4.2 \mu\text{m}$, while $\text{Ave}(90\%) = 28.4 \pm 5.6 \mu\text{m}$. The rms spot diameters at the center of each order are shown for all orders in Table 8.

5.1.2. Measured System Performance

After assembly and integration into the Keck II telescope, a series of optical tests was performed to assess the optical performance of the instrument. In the imaging mode, optical performance was analyzed by imaging an array of pinholes placed in the slit-mask location. In the LDP mode, a linear array of pinholes was used, and in the echelle mode, a single pinhole was used. The pinholes are $125 \mu\text{m}$ in diameter, which projects to $16.8 \mu\text{m}$ at the detector apart from anamorphic factors (compared to $15 \mu\text{m}$ pixels). Thus, they contribute slightly to measured spot sizes. The pinholes were illuminated by either the dome floodlamps or the internal quartz-halogen flat lamp. The case of dome illumination most accurately mimics the star illumination as the Keck II pupil is imaged into ESI. In the case of internal flat-field lamps, internal baffles become the system stop. These apertures are larger than the Keck pupil and are not hexagonal. Thus, the artificial source tests overestimate the image sizes as a result of overfilling of the camera pupil. For the case of imaging mode, the standard filter set provided with

TABLE 7
ECHELLETTE-MODE MODEL TERMS AND STATISTICS

Term	1999 October	1999 November	2001 March No. 1	2001 March No. 2
a_0	1397.24	1382.72	1328.05	1327.90
a_1	1.498 ± 0.049	1.577 ± 0.054	1.663 ± 0.076	1.588 ± 0.078
a_2	1.544 ± 0.051	1.632 ± 0.051	1.576 ± 0.069	1.537 ± 0.070
a_3	3.278 ± 0.064	3.074 ± 0.068	3.345 ± 0.092	3.496 ± 0.095
σ_x	0.20 pixels	0.21 pixels	0.20 pixels	0.21 pixels
b_0	2023.98	2024.08	2027.13	2027.25
b_1	-2.088 ± 0.037	-2.024 ± 0.037	-2.027 ± 0.052	-1.884 ± 0.102
b_2	0.561 ± 0.039	0.583 ± 0.035	0.542 ± 0.047	0.636 ± 0.092
b_3	0.316 ± 0.049	0.503 ± 0.047	0.481 ± 0.063	0.314 ± 0.124
σ_y	0.15 pixels	0.15 pixels	0.14 pixels	0.27 pixels

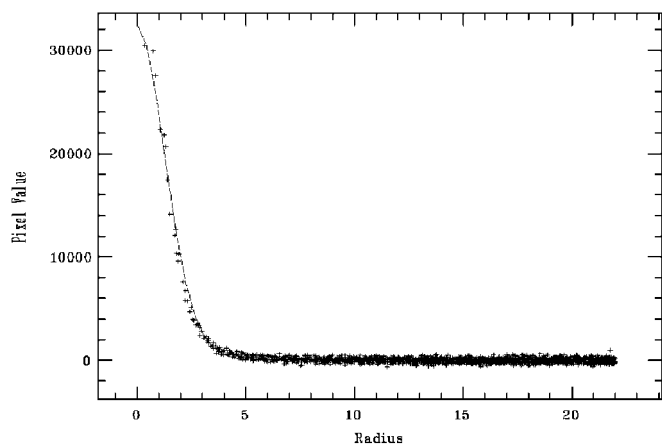


FIG. 11.—*I*-band image of the globular cluster Palomar 13 azimuthally averaged and fitted to a Gaussian energy distribution. The FWHM of this particular star image is $0''.34$, which is approximately the median value for all stars in this image. The figure demonstrates that the image quality of ESI shows no asymmetries even under the best seeing conditions.

ESI (Johnson *B* and *V*, Spinrad *R*, and Gunn *I*) and no-filter were used. In all cases, a series of images was taken at a range of focus settings.

Image quality was determined by fitting each spot to a two-dimensional azimuthally averaged Gaussian distribution using IDL. The radial profiling routine returns the standard deviation for each fitted Gaussian. These were converted to the two-dimensional rms spot diameters (D_{rms}) by multiplying the standard deviation by 2.828. The D_{rms} was determined for a variety of wavelengths as a function of focal position in the two spectroscopic modes. In the imaging mode, D_{rms} was determined for a variety of field positions as a function of focal position. These D_{rms} values were computed as the median over location on the chip of the D_{rms} values as a function of camera focal position. These data are plotted in Sheinis et al. (2000).

The D_{rms} at best focus is compared to that predicted for the design in Table 8. The data in Table 8 show a discrepancy between design prediction and measured D_{rms} . This discrepancy is due in part to the fabrication and assembly errors included in the error budget, and due to a small additional error ascribed the improper illumination in the testing, as mentioned above. This assertion is based on the results of the globular cluster tests below and the initial camera testing, which imply better performance than this artificial star test.

Testing on the sky was done by observing several globular clusters in *BVR* under good seeing conditions. The FWHM was calculated for each image using the IRAF image reduction package. This was done by fitting the azimuthally averaged images to Gaussian energy distributions. The quality of the fit and the FWHM of the fitted images are displayed in Figures 11 and 12.

The average *I*-band images show an FWHM of $0''.34$. This is consistent with a measured instrumental FWHM of $0''.23$ (Sheinis et al. 2000) convolved with an inferred FWHM seeing

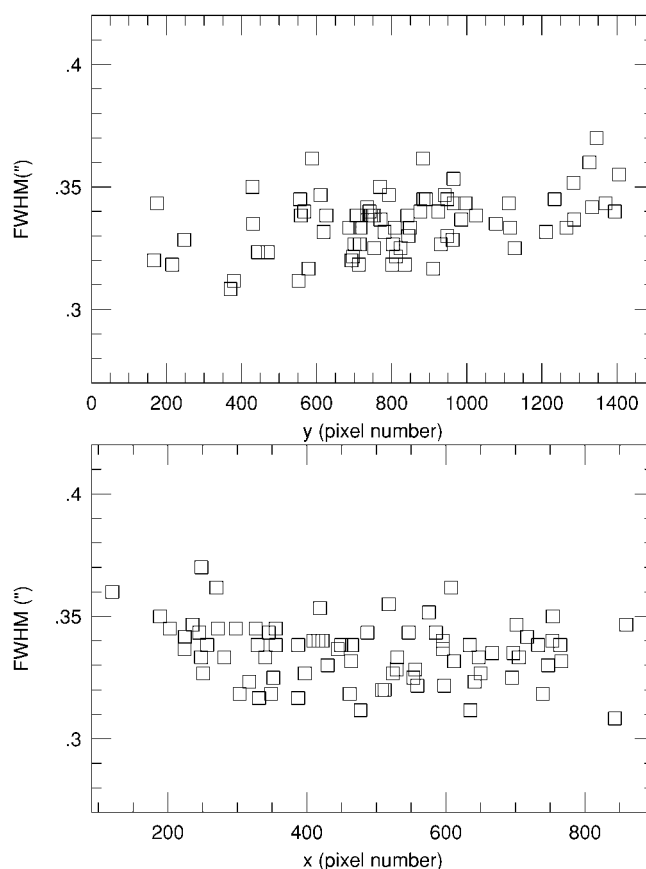


FIG. 12.—FWHM distribution of *I*-band image of the globular cluster Palomar 13 plotted as a function of *X* and *Y* pixel number on the detector. This figure demonstrates that ESI produces no observable variation in spot diameter as a function of image position on the detector.

disk of $0''.25$ assuming no guiding errors. These are the best non-adaptive optics (AO) optical images at Keck to date.

5.2. Efficiency

5.2.1. Instrument Efficiency in Echellette Mode

Observations of the spectrophotometric standard Wolf 1348 were made through a $6''.0$ wide slit during the 1999 September commissioning run. The observations were corrected for an air mass of 1.04 using the mean extinction curve for Mauna Kea downloaded from the Canada-France-Hawaii WWW site. The values for flux/wavelength for Wolf 1348 were taken from the tables of Massey et al. (1988) and Massey & Gronwall (1990) and converted into photons $\text{s}^{-1} \text{\AA}^{-1}$ using the relation

$$N_{\lambda} = \frac{4.275X \times 10^{12}}{\lambda} 10^{-(m_{\lambda} + A_{\lambda}X)/2.5}.$$

Here m_{λ} is the magnitude from the Massey et al. (1988) tables, A_{λ} is the extinction in magnitudes per air mass at λ , X is the air mass of the observation, and λ is the wavelength in \AA .

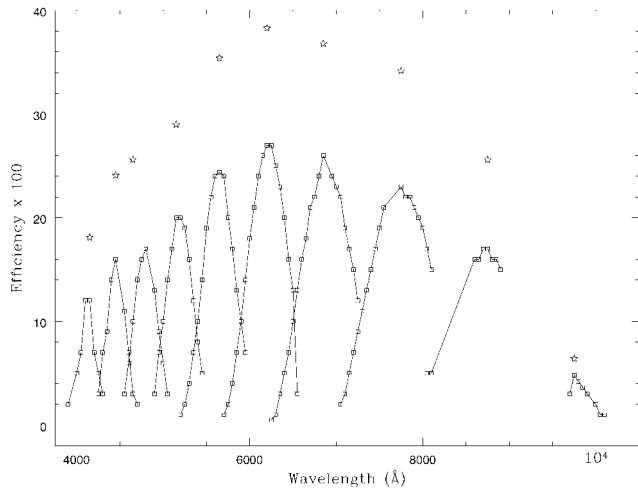


FIG. 13.—Ratio of the number of photons predicted for Wolf 1348 to the number detected (corrected to the top of the atmosphere) for the echellette mode including the detector and telescope losses. The solid line connecting open squares is the measured efficiency for each order after removing the effects of atmospheric extinction. The five-point stars show the total *instrument* efficiency at the peak of each order after backing out the effects of two reflections off aluminum surfaces. The plots show efficiency calculated order by order (that is, not summing the flux at a given wavelength that is detected in more than one order). For the bluer orders, adding flux from adjacent orders at common wavelengths increases the overall throughput at some wavelengths by as much as a factor of 1.6.

Figure 13 shows the ratio of the number of photons predicted for Wolf 1348 to the number detected (corrected to the top of the atmosphere) for the echellette mode including the detector and telescope losses. The solid line connecting open squares is the measured efficiency for each order after removing the effects of atmospheric extinction. The five-pointed stars show the total *instrument* efficiency at the peak of each order after backing out the effects of two reflections off of aluminum surfaces. The aluminum efficiency curve for the secondary assumed “fresh” aluminum. This was reduced by 5% for the primary, which was known to have been degraded by at least that amount by the time of the observation. The plot shows efficiencies calculated order by order (that is, not summing the flux at a given wavelength that is detected in more than one order). For the bluer orders, adding flux from adjacent orders at common wavelengths would increase the overall throughput at some wavelengths by as much as a factor of 1.6.

5.2.2. Instrument Efficiency in LDP Mode

Figure 14 shows the ratio of the number of photons predicted for Wolf 1348 to the number detected (corrected to the top of the atmosphere) for the prismatic (LDP) mode including the detector and telescope loss. The solid line is the measured efficiency after removing the effects of atmospheric extinction.

The peak efficiency in LDP mode has been measured to be at least a factor of 1.4 better than in the echellette mode. The

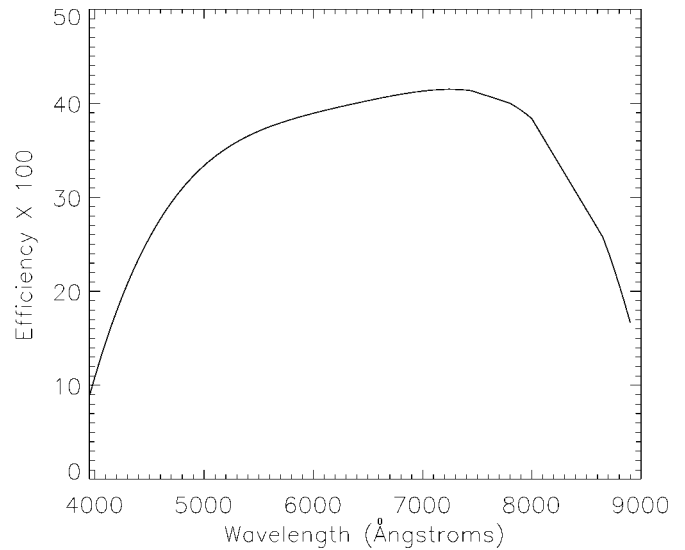


FIG. 14.—Ratio of the number of photons predicted for Wolf 1348 to the number detected (corrected to the top of the atmosphere) for the prismatic (LDP) mode including the detector and telescope losses. The solid line is the measured efficiency after removing the effects of atmospheric extinction.

greater efficiency in LDP mode is due primarily to the greater reflectivity of the LDP fold mirror as compared with the grating. The beam in LDP mode shares a common path with the echellette mode except for this fold mirror, which replaces the grating in LDP mode.

6. CONCLUSIONS

We have discussed the design, engineering development, construction, and implementation of the ESI spectrograph. We have given an overview of all of the major subsystems together with the most important of the design criteria. Performance has been analyzed in terms of throughput, image diameters, and residual flexure. Imaging studies of globular clusters have produced the best non-AO visible images to date at Keck Observatory. Throughput of the telescope and the instrument (including the CCD detector) in echellette mode has been observed to be as high as 28% in echellette mode and greater than 41% in LDP mode.

The authors wish to thank the entire technical staff at Lick Observatory, including (in no particular order) the following: in the Electronics Laboratory, Barry Alcott, Ted Cantrall, Carol Harper, and Jim Burrous (deceased); in the Instrument Laboratory, Jeff Lewis, Dick Kanto, Terry Pfister, Jim Ward, and Gary Dorst; in the Optical Laboratory, David Hilyard; in the engineering department, David Cowley, Carol Osborne, Jack Osborne, Vern Wallace, Chris Wright, Mary Poteete, and Heather Mietz; in the Software Development Laboratory, De Clark, Steve Allen, and Dean Tucker; in the Detector Development Laboratory, Richard Stover, Mingzhi Wei, Kirk Gil-

more, Bill Brown, and Lloyd Robinson; and in the business office, Maureen McLean, Marlene Couture, and Edna Sandberg.

The authors also wish to thank Jerry Nelson and Terry Mast

for their many insightful comments and suggestions. We would especially like to thank Bob Goodrich and the staff at Keck Observatory for their help with the assembly, testing, and data acquisition for this instrument.

REFERENCES

- Becker, R. H., et al. 2000, *AJ*, 122, 2850
- Bigelow, B. C., & Nelson, J. E. 1998, *Proc. SPIE*, 3355, 164
- Burke, B. E., et al. 2000, in *Optical Detectors for Astronomy II: State-of-the-Art at the Turn of the Millenium*, ed. P. Amico & J. W. Beleticpp (Boston: Kluwer), 187
- Epps, H. W. 1998, *Proc. SPIE*, 3355, 111
- Epps, H. W., & Miller, J. S. 1998, *Proc. SPIE*, 3355, 48
- Hilyard, D. F., Laopodis, G. K., & Faber, S. M. 1999, *Proc. SPIE*, 3786, 482
- Kibrick, R. I., Miller, J. S., Nelson, J. E., Radovan, M. V., Sheinis, A. I., & Sutin, B. M. 2000, *Proc. SPIE*, 4009, 262
- Leach, R. W., Beale, F. L., & Eriksen, J. E. 1998, *Proc. SPIE*, 3355, 512
- Massey, P., & Gronwall, C. 1990, *ApJ*, 358, 344
- Massey, P., Strobel, K., Barnes, J. V., & Anderson, E. 1988, *ApJ*, 328, 315
- Oke, J. B., et al. 1994, *Proc. SPIE*, 2198, 178
- Prochaska, J. X., Gawiser, E., & Wolfe, A. M. 2001, *ApJ*, 552, 99
- Radovan, M. V., Bigelow, B. C., Nelson, J. E., & Sheinis, A. I. 1998, *Proc. SPIE*, 3355, 155
- Sheinis, A. I., Miller, J. S., Bolte, M., & Sutin, B. M. 2000, *Proc. SPIE*, 4008, 522
- Sheinis, A. I., Nelson, J. E., James, E. C., & Radovan, M. V. 1999a, *Proc. SPIE*, 3786, 350
- Sheinis, A. I., Nelson, J. E., & Radovan, M. V. 1998, *Proc. SPIE*, 3355, 59
- Sheinis, A. I., Sutin, B. M., Epps, H. W., Schier, J. A., Hilyard, D. F., & Lewis, J. 1999b, *Proc. SPIE*, 3786, 413
- Sutin, B. M. 1997, *Proc. SPIE*, 2871, 1116